

Statistical survey of widely spread out solar electron events observed with STEREO and ACE with special attention to anisotropies[★]

N. Dresing¹, R. Gómez-Herrero², B. Heber¹, A. Klassen¹, O. Malandraki³, W. Dröge⁴, and Y. Kartavykh^{4,5}

¹ Institut für Experimentelle und Angewandte Physik, Christian-Albrechts-Universität zu Kiel, Germany
e-mail: dresing@physik.uni-kiel.de

² Space Research Group, University of Alcalá, Spain

³ IAASARS, National Observatory of Athens, Greece

⁴ Institut für Theoretische Physik und Astrophysik, Universität Würzburg, Germany

⁵ Ioffe Physical-Technical Institute, St.-Petersburg, Russia

Received 10 March 2014 / Accepted 12 May 2014

ABSTRACT

Context. In February 2011, the two STEREO spacecrafts reached a separation of 180 degrees in longitude, offering a complete view of the Sun for the first time ever. When the full Sun surface is visible, source active regions of solar energetic particle (SEP) events can be identified unambiguously. STEREO, in combination with near-Earth observatories such as ACE or SOHO, provides three well separated viewpoints, which build an unprecedented platform from which to investigate the longitudinal variations of SEP events.

Aims. We show an ensemble of SEP events that were observed between 2009 and mid-2013 by at least two spacecrafts and show a remarkably wide particle spread in longitude (wide-spread events). The main selection criterion for these events was a longitudinal separation of at least 80 degrees between active region and spacecraft magnetic footpoint for the widest separated spacecraft. We investigate the events statistically in terms of peak intensities, onset delays, and rise times, and determine the spread of the longitudinal events, which is the range filled by SEPs during the events. Energetic electron anisotropies are investigated to distinguish the source and transport mechanisms that lead to the observed wide particle spreads.

Methods. According to the anisotropy distributions, we divided the events into three classes depending on different source and transport scenarios. One potential mechanism for wide-spread events is efficient perpendicular transport in the interplanetary medium that competes with another scenario, which is a wide particle spread that occurs close to the Sun. In the latter case, the observations at 1 AU during the early phase of the events are expected to show significant anisotropies because of the wide injection range at the Sun and particle-focusing during the outward propagation, while in the first case only low anisotropies are anticipated.

Results. We find events for both of these scenarios in our sample that match the expected observations and even different events that do not agree with the scenarios. We conclude that probably both an extended source region at the Sun and perpendicular transport in the interplanetary medium are involved for most of these wide-spread events.

Key words. Sun: corona – Sun: flares – Sun: particle emission – shock waves – scattering – diffusion

1. Introduction

Solar energetic particle (SEP) events are of great interest because they allow unique insights into particle acceleration, injection, and transport mechanisms in the inner heliosphere. Energy spectra, time series of intensity and anisotropy, and ionic charge states are signatures of acceleration, injection, and transport. Multispacecraft observations from well separated points do not only prove an event at a certain angular distance, but provide information on the actual angular spread of the event at a certain distance to the Sun. Helios observations revealed that the angular spread in the inner heliosphere can be very different, ranging from tens of degrees to more than 180 degrees (Kallenrode 1993; Reames 1999; Torsti et al. 1999; Cliver et al. 2005; Wibberenz & Cane 2006).

Flaring active regions at the Sun are believed to be strong particle accelerators that produce impulsive, electron- and ³He-rich events (Lin & Hudson 1976; Hsieh & Simpson 1970). Because they are very confined regions, these sources are expected to lead to narrow longitudinal spreads inside the inner

heliosphere if the SEPs simply propagate outwards along the magnetic field spirals that are connected to the source active region (e.g., Klassen et al. 2012). Recent observations from the STEREO mission reported by Wiedenbeck et al. (2013), however, question the constraint of a narrow spread of ³He-rich events. Wider angular particle distributions and especially extremely wide spreads of SEPs (wide-spread events) that indicate distributions all around the Sun (i.e., Dresing et al. 2012), are even more challenging to understand, and several ideas and processes have been proposed to explain these observations. These processes may be separated into two categories that operate predominantly close to the Sun (in the corona) or in the interplanetary (IP) medium. The former includes coronal shocks that accelerate particles in a large spatial region or efficient transport processes in the corona. Several mechanisms have been proposed for the coronal transport, for example, diverging magnetic field lines below the source surface (Klein et al. 2008) or different coronal diffusion (Reinhard & Wibberenz 1974; Newkirk & Wentzel 1978), which provides a pre-spreading of tens of degrees before the particles enter the open magnetic field lines and escape into the IP medium. The presence of so-called EIT waves has also been introduced to be responsible for the spread of SEP

[★] Appendix A is available in electronic form at <http://www.aanda.org>

events (Krucker et al. 1999; Rouillard et al. 2012; Park et al. 2013). These EIT waves are seen as coronal disturbances in EUV images, that were first observed with the EIT instrument onboard SOHO (Moses et al. 1997; Thompson et al. 1998).

By the end of the 1990s, events with wider spreads were classified as gradual, not flare-associated events. These proton-rich events were associated with CME-driven shocks that build an extended source region in the IP medium (Mason et al. 1984; Cane et al. 1986; Kallenrode 1993; Reames 1999). Another mechanism operating in the IP medium that might provide a large SEP spread is strong and efficient transport perpendicular to the mean magnetic field (Dalla et al. 2003; Dröge et al. 2010; Laitinen et al. 2013; Marsh et al. 2013). In this sense, both the random walk of magnetic field lines and perpendicular diffusion caused by scattering can contribute to the lateral transport. Furthermore, pre-event ICMEs, large magnetic loops, and transient structures can perturb and deform the IP magnetic field structure and modify the nominal connectivity (cf. Richardson et al. 1991; Gómez-Herrero et al. 2006; Leske et al. 2012; Lario et al. 2013).

To separate these processes, very specific and comprehensive observations are required. In addition to in-situ measurements, remote-sensing observations are indispensable to clearly identify the source region at the Sun. Multiple viewpoints well-separated in space are also very important to study angular variations and the angular spread of the event. These viewpoints should be situated at the same radial distance to exclude radial gradient effects. These requirements are all fulfilled by the twin STEREO spacecraft (s/c), which constitute an excellent and unique platform to study SEP events especially when complemented with close-to-Earth spacecraft (such as SOHO, ACE, and SDO) and ground-based observations.

In this work we investigate a set of near relativistic solar energetic electron events that show a remarkable longitudinal distribution. We chose a statistical approach and investigated the longitudinal variation of event properties such as highest intensities, onset delays, and rise times of these extreme events. As a key information we investigated the anisotropies that are observed at different viewpoints. With this information we discuss the role and importance of the different transport and injection mechanisms that can lead to the large observed longitudinal spread.

2. Instrumentation

The electron observations used in this work are provided by the Solar Electron and Proton Telescope (SEPT, Müller-Mellin et al. 2008) onboard the STEREO spacecraft and the Electron Proton and Alpha Monitor (EPAM) onboard ACE (Gold et al. 1998). The SEPT instrument measures electrons in the range of 45–400 keV. It consists of four identical telescopes mounted to cover four viewing directions, which are to the north, to the south, along the nominal Parker spiral to the Sun, and away from the Sun. ACE/EPAM measures the flux and direction of electrons and protons. The LEFS60 telescope provides 40 keV to about 350 keV electron measurements, and by the spinning of the spacecraft the measurements are divided into eight different directional sectors. Complementary information on plasma properties are provided by the STEREO/PLASTIC (Galvin et al. 2008) and ACE/SWEPAM (McComas et al. 1998) instruments. The interplanetary magnetic field measurements by STEREO/MAG (Acuña et al. 2007) and ACE/MAG (Smith et al. 1998) are investigated to determine the pitch angle distributions and particle anisotropies. To link in-situ observations

with the associated active regions (AR) at the Sun we evaluated images taken by the SECCHI investigation (Howard et al. 2008) in extreme-ultraviolet (EUVI) and coronagraphic observations (COR1 and COR2 instruments) provided by the STEREO spacecraft. EUV observations by SDO/AIA (Lemen et al. 2012) and the coronagraph LASCO (Brueckner et al. 1995) on board the SOHO spacecraft complete these observations. The occurrence of CMEs and their key parameters such as the CME speed and width can be found in the SOHO LASCO CME Catalog¹ or in the CACTus CME lists², which also provide lists for STEREO A and STEREO B observations. Radio (type II and type III) bursts are observed with the WAVES instrument onboard WIND (Bougeret et al. 1995) and the STEREO/WAVES instruments (Bougeret et al. 2008) at frequencies ≤ 16 MHz.

3. Event selection and overview

The increasing longitudinal separation of the two STEREO spacecraft from Earth provided progressively wider imaging coverage of the solar atmosphere until February 2011, when the STEREOs reached a separation of 180 degrees from each other, making the full Sun visible at once for the first time ever. In contrast to the Helios era, backside events as seen from one spacecraft can now be unambiguously linked to the parent active region when employing another spacecraft that observes the event from the front side. With this 360° view one can not only study the longitudinal variation of event parameters, but also identify and investigate wide-spread SEP events. Multispacecraft STEREO observations of the same event also allow one to estimate the actual longitudinal width of the SEPs at 1 AU, which we call the longitudinal event width (see Dresing et al. 2013).

To collect a list of wide-spread events, we scanned the whole STEREO dataset beginning with the nominal mission in January 2007 up to mid-2013. The events were selected according to the following criteria:

- (1) an electron increase in the energy range of 55–105 keV above background has to be detected by at least two of the three spacecraft, and
- (2) the widest separated spacecraft must have a flare to s/c footpoint longitudinal separation of at least 80 degrees.

Several event candidates had to be excluded from the list because strong ion contamination masked the electron event or because an unambiguous identification of the source AR was not possible because of additional type III and flare candidates.

The longitudinal coordinates of the spacecraft magnetic footpoints at the Sun were calculated assuming a Parker spiral and taking into account the measured solar wind speed during the event onset. The latitude of the s/c footpoint is equal to the s/c latitude. The coordinates of the flare were determined using EUV images and movies taken by STEREO/EUVI and SDO/AIA.

Table 1 presents the event numbers, dates, and associated type III radio burst onset times in Cols. 1 to 3. We considered the type III onset (at ~ 14 MHz measured by STEREO/WAVES and WIND/WAVES) as the expected solar injection time instead of the flare start time. The source Carrington longitude of the associated flare and the longitudinal separation angles of the magnetic footpoints of the spacecraft to the flare longitude are listed in Cols. 4 to 7. While positive values denote source regions situated to the west of the spacecraft magnetic footpoints, negative

¹ http://cdaw.gsfc.nasa.gov/CME_list/

² <http://sidc.oma.be/cactus/>

Table 1. Event number, date, type III radio burst onset time, Carrington longitude (CL) of the flare, longitudinal separating angles between the s/c footprint and the flaring AR.

No.	Date	Type III onset (UT)	Flare CL	Longitudinal separation angle (°)			Associated phenomena			
				STB	ACE	STA	CME speed (km s ⁻¹)	CME width (°)	type II burst	EUV wave
1	2009-11-03	03:31	215	105	62	3	0	0	0	1
2	2010-01-17	03:54	54	-112	165	118	532 (B)	90	1	1
3	2010-02-07	02:29	255	7	-78	-121	421 (S)	142	0	1
4	2010-02-12	11:24	180	-32	-87	-129	568 (B)	92	1*	1
5	2010-08-07	18:11	350	-40	-96	-160	871 (S)	142	1	1
6	2010-08-14	10:01	350	45	-5	-92	1205 (S)	148	1	1
7	2010-08-18	05:32	350	92	36	-42	1471 (S)	184	1	1
8	2010-08-31	20:48	213	133	72	17	892 (A)	100	1	1
9	2010-09-09	23:22	52	90	25	-50	818 (S)	147	1	1
10	2011-02-24	07:30	177	-27	-154	115	1186 (S)	158	1	1
11	2011-11-03	22:14	10	-133	137	13	781 (A)	216	1	1
12	2011-11-26	07:14	275	87	-12	-115	933 (S)	190	1	1
13	2012-01-23	03:40	208	61	-32	-152	1136 (A)	120	1	1
14	2012-03-07	00:17	300	18	-94	163	961 (B)	352	1	1
15	2012-04-15	02:10	73	-27	-151	89	1644 (cS)	160	1	DG
16	2012-04-16	17:25	73	1	-150	111	822 (cS)	80	0	1
17	2012-05-17	01:31	190	141	16	-89	1302 (cS)	200	1	1
18	2012-08-31	19:50	90	-11	-111	128	651 (cS)	210	1	1
19	2013-03-05	03:16	73	-98	156	18	1316 (S)	360	1	1
20	2013-04-11	06:58	71	64	-77	153	694 (B)	348	1	1
21	2013-06-21	02:48	160	9	-132	91	1249 (cS)	160	1	1

Notes. DG: data gap. CME speed and width if accompanied by a CME, and associated type II radio bursts and EIT waves. CME speed and width have been taken from the SOHO LASCO CME catalog (marked with (S)), or the CACTus catalogs (see Sect. 2), where (B) means STEREO B, (A) means STEREO A, and (cS) stands for SOHO. The type II radio burst marked by * was only observed at high frequencies >200 MHz by a ground-based station (BLEN).

values represent a source to the east. The last four columns show the CME speed and width and presence of a type II radio burst or an EIT wave. All but one of the events were accompanied by a CME, 18 events (86%) were associated with a type II radio burst, indicating the presence of a shock, and all events were accompanied by an EIT wave (with one event being unclear because of a data gap (DG) in SDO/AIA).

In Fig. 1 the longitudinal configurations of flare and spacecraft positions are sketched for each of the events listed in Table 1. The longitude of the flaring active region is marked by the arrow, the dotted black spiral is the nominal Parker field line connecting to the active region. The colored spirals and dotted lines mark the field lines that connect the spacecraft to the Sun and their longitudinal positions.

Columns 1 to 3 of Table 2 are the same as in Table 1. The next three columns show the 55–105 keV electron onset times at the spacecraft, and Cols. 7 to 9 list the maximum times of the events at the three spacecraft. The maxima of the events were identified using 10-min averages, and local phenomena such as shock spikes or pitch-angle changes due to magnetic field variations were excluded when we determined the maximum time. For some events affected by shocks we used different viewing sectors to identify the onset and maximum times. The peak intensity was corrected for by a pre-event background subtraction. With an energy bin of 53–103 keV, the ACE/EPAM data are well comparable with the STEREO/SEPT measurements of 55–105 keV electrons. However, an intercalibration factor of 1/1.3 (cf. Lario et al. 2013) was applied to the ACE data to incorporate the different instrument responses. Figure 2 illustrates how we determined onset and time to maximum for the example of the 7 March 2012 event observed by STEREO A. The first vertical line labeled t_{inj} marks the onset time of the type III radio

burst, the second line (t_{ons}) marks the onset time of the electron increase, and the last line (t_{max}) represents the maximum time determined for this event. Note that the maximum has been identified as the first maximum although the later maximum around day of year 67.3 is slightly higher. The delay between t_{ons} and t_{max} is the rise time of the event Δt .

To ensure that all the spacecraft observations were associated with the same event, all events were checked carefully for other possible source regions such as flares or type III radio bursts close in time. If this was unclear, the events were excluded.

Table 3 lists the event numbers, dates, peak intensities detected at each of the spacecraft, and the anisotropy class defined in Sect. 4.3.

4. Data analysis

4.1. Longitudinal variation of peak intensities and event width

Figure 3 shows the peak intensities (as listed in Table 3) of each event detected by each s/c as a function of the longitudinal separation angle. A separation angle of 0 denotes a perfect connection, meaning that the s/c and the source active region are directly connected by a Parker magnetic field line according to the measured solar wind speed. Different symbols mark the different spacecraft, and each color stands for a specific event. If a spacecraft did not observe an intensity increase, the point was set onto the horizontal axis to indicate the longitudinal separation angle of this spacecraft. The same was done for ambiguous events, which were excluded (cf. Tables 2 and 3).

For those of the 21 wide-spread events that had three points, we approximated the longitudinal distribution of peak intensities

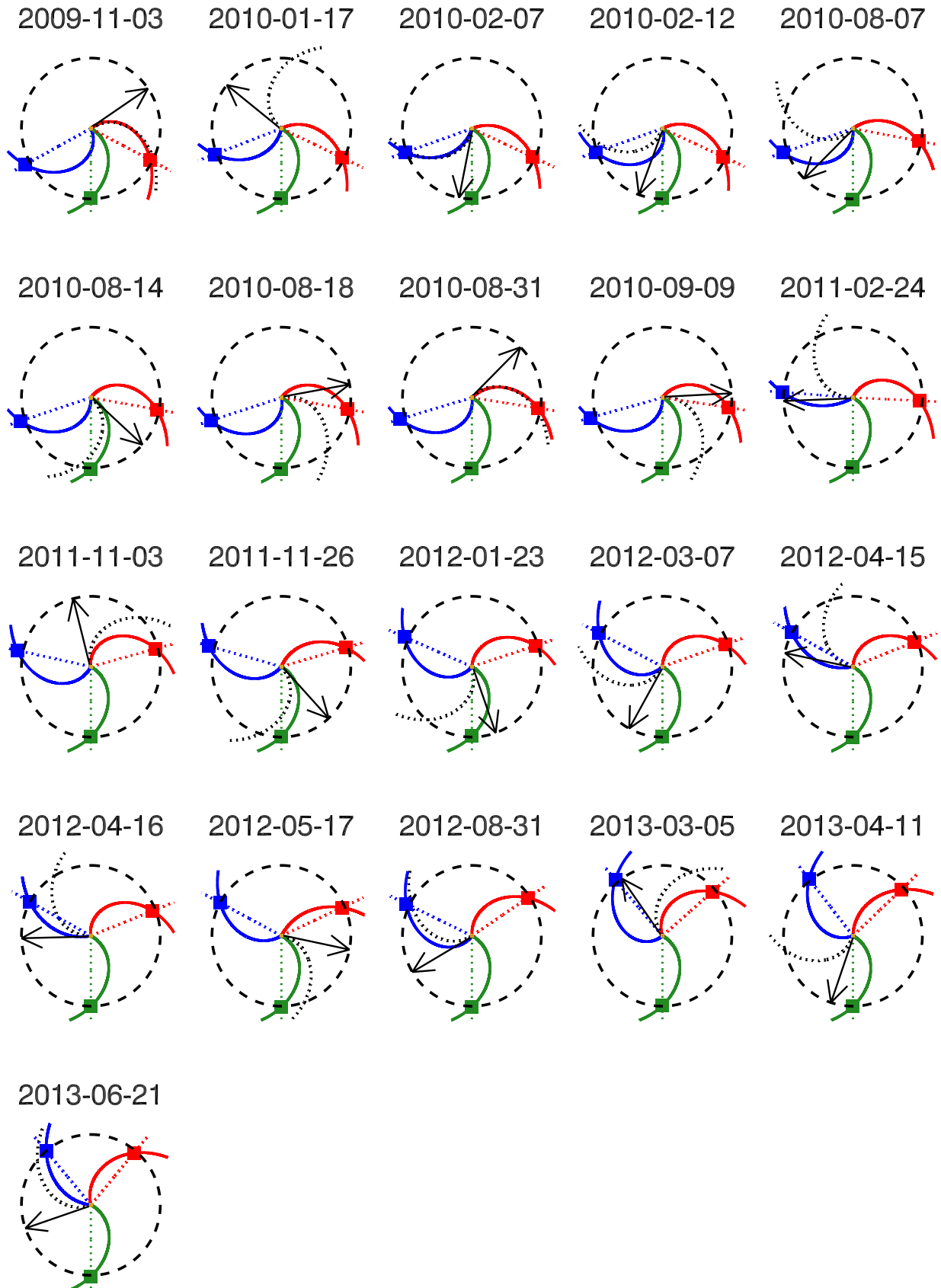


Fig. 1. Longitudinal configurations of spacecraft and source active regions for each of the analysed events. The arrow marks the longitude of the flaring source active region, the dotted black spiral is the nominal Parker field line originating from the source region. The colored spirals represent the magnetic field lines connecting the spacecraft to the Sun, corresponding to the measured solar wind speed. The dotted colored lines mark the longitudinal positions of each spacecraft, where blue marks STEREO B, red STEREO A, and green ACE.

Table 2. Event number, date, type III radio burst onset times, onset and maximum times of 55–105 keV electrons at the three spacecrafts.

No.	Date	Type III onset (UT)	Electron onset time (UT)			Electron maximum time (UT)		
			STB	ACE	STA	STB	ACE	STA
1	2009-11-03	03:31	06:44	03:54	03:57	09:55	05:50	04:25
2	2010-01-17	03:54	04:30	NE	04:55	13:35	NE	09:35
3	2010-02-07	02:29	03:04	03:00	05:32	03:45	06:35	12:35
4	2010-02-12	11:24	12:14	12:20	13:04	13:15	13:15	15:45
5	2010-08-07	18:11	19:07	19:32	NE	22:35	20:55	NE
6	2010-08-14	10:01	10:30	10:18	10:52	11:35	11:05	12:25
7	2010-08-18	05:32	06:53	06:16	06:10	07:35	08:25	07:05
8	2010-08-31	20:48	22:07	21:29	21:21	22:15	02:15*	23:05
9	2010-09-08	23:22	AM	00:10*	NA	06:15*	01:15*	NA
10	2011-02-24	07:30	08:19	NE	12:12	12:45	NE	13:55
11	2011-11-03	22:14	23:24	23:08	22:42	12:15*	01:05*	01:15*
12	2011-11-26	07:14	08:15	07:27	IC	12:25	09:45	IC
13	2012-01-23	03:40	NA	04:00	07:45	NA	06:05	AM
14	2012-03-07	00:17	00:59	01:45	01:38	01:55	14:35	04:15
15	2012-04-15	02:10	02:38	NE	03:03	06:45	NE	06:25
16	2012-04-16	17:25	17:58	NE	18:35	19:05	NE	20:35
17	2012-05-17	01:31	04:35	01:48	07:15	13:45	02:45	IC
18	2012-08-31	19:50	20:11	21:08	03:50*	21:55	01:05*	19:15*
19	2013-03-05	03:16	05:15	09:50	03:40	23:05	10:35*	04:45
20	2013-04-11	06:58	07:24	07:52	14:15	09:05	10:25	AM
21	2013-06-21	02:48	03:14	07:55	05:50	03:55	AM	08:05

Notes. Times marked by a * occurred on the next day. AM: ambiguous, no maximum, if rise takes too long and other type III bursts follow; or no onset because the increase is too weak. IC: ion contamination saturates the electron measurement. NE: no event detected. NA: there is an increase, but likely not associated with the event.

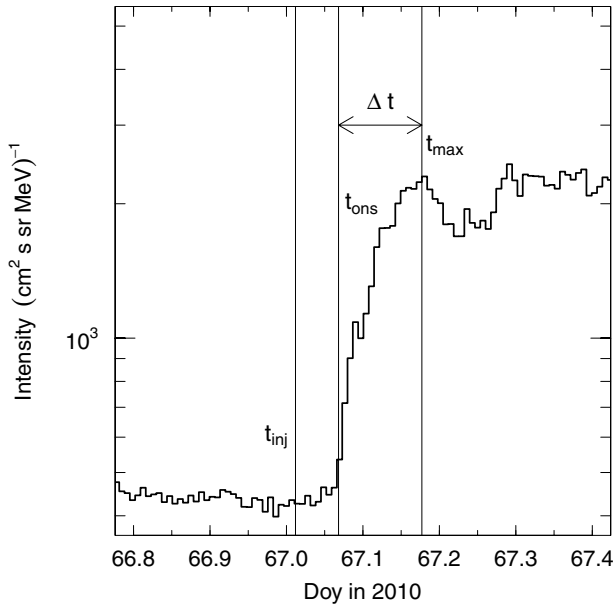


Fig. 2. Onset and maximum time determination for STEREO A observations of the 7 Mar. 2012 event. The increase in 55–105 keV electrons has been detected by the SEPT instrument in the Sun sector. The three horizontal lines mark (from left to right) the type III radio burst onset time (t_{inj}), the electron onset time (t_{ons}), and the electron maximum time (t_{max}) (cf. Table 2). The rise time of the event is the time from electron onset to electron maximum (Δt).

with Gaussian functions:

$$I(\phi) = I_0 \exp[-(\phi - \phi_0)^2 / 2\sigma^2]. \quad (1)$$

Here, I_0 represents the peak intensity at 1 AU and zero degrees separation angle ϕ , and σ is the standard deviation. ϕ_0 is the

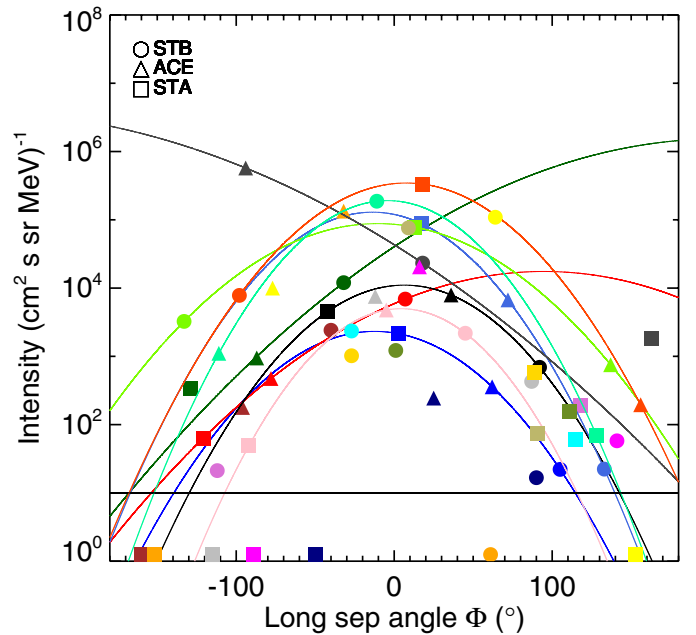


Fig. 3. Peak intensities as a function of longitudinal separation angle. Positive separation angles denote a source to the west, negative angles mark a source to the east of the spacecraft magnetic footprint. Observations of the same event are marked by the same color. Points lying on the horizontal axis denote that there were no observations because of various reasons (cf. Tables 2 and 3). The curves represent Gaussian fits (Eq. (1)) for the three-spacecraft events.

center of the Gaussian. The colored curves in Fig. 3 are approximations of Eq. (1) to each of the three-spacecraft events. Since for most of the events Eq. (1) approximates the data points well, the σ -distribution shown in Fig. 4 can be understood as

Table 3. Event number, date, peak intensities of 55–105 keV electrons at the three spacecrafts, and anisotropy class of the event (see Sect. 4.3).

No.	Date	Peak intensity (cm ² sr MeV) ⁻¹			Anisotropy class
		STB	ACE	STA	
1	2009-11-03	2.21E+01	4.65E+02	2.14E+03	1
2	2010-01-17	2.12E+01	NE	1.91E+02	1
3	2010-02-07	6.90E+03	6.16E+02	6.28E+01	2
4	2010-02-12	1.20E+04	1.23E+03	3.34E+02	2
5	2010-08-07	2.41E+03	2.32E+02	NE	1
6	2010-08-14	2.18E+03	6.21E+03	4.88E+01	3
7	2010-08-18	6.91E+02	1.03E+04	4.55E+03	3
8	2010-08-31	2.23E+01	8.73E+03	8.84E+04	2
9	2010-09-08	1.67E+01	3.18E+02	NA	1
10	2011-02-24	2.35E+03	NE	6.04E+01	3
11	2011-11-03	3.25E+03	9.80E+02	7.80E+04	3
12	2011-11-26	4.29E+02	9.81E+03	IC	1
13	2012-01-23	NA	1.74E+05	AM	1
14	2012-03-07	2.32E+04	7.45E+05	1.85E+03	2
15	2012-04-15	1.02E+03	NE	5.72E+02	1
16	2012-04-16	1.22E+03	NE	1.54E+02	2
17	2012-05-17	5.79E+01	2.66E+04	IC	1
18	2012-08-31	1.87E+05	1.44E+03	7.04E+01	1
19	2013-03-05	7.81E+03	2.54E+02	3.33E+05	1
20	2013-04-11	1.09E+05	1.30E+04	AM	2
21	2013-06-21	7.61E+04	AM	7.45E+01	2

Notes. The peak intensities at ACE have been corrected for by an intercalibration factor of 1/1.3 (see text). AM: ambiguous, no maximum, if rise takes too long and other type III bursts follow; or no onset because the increase is too weak. IC: ion contamination saturates the electron measurement. NE: no event detected. NA: there is an increase, but likely not associated with the event.

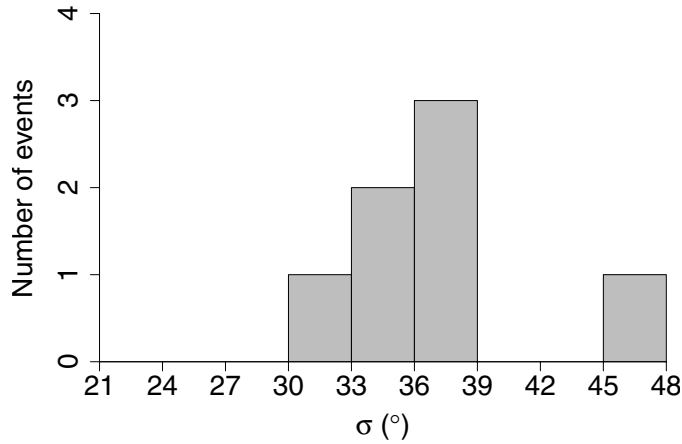


Fig. 4. Distribution of σ -values of the fits shown in Fig. 3, where fits yielding a $|\phi_0| > 90^\circ$ were excluded.

a representation of possible values. Note that we excluded fits revealing a $|\phi_0| > 90^\circ$ as poor fits here. We found a wide variety in the standard deviation σ between 32° and 48° degrees with a mean of 37.3° degrees (not taking into account two-spacecraft events and the events with $|\phi_0| > 90^\circ$, which leaves seven events).

In a similar investigation, Lario et al. (2013) studied 35 STEREO multispacecraft SEP events and found a standard deviation σ of $49 \pm 2^\circ$ and an asymmetry of $\phi_0 = -16^\circ$ to the east for 71–112 keV electron events. Although we investigate widespread events in this paper, our value of $\sigma = 37.3^\circ$ is significantly lower than the one found by Lario et al. (2013). If we had applied the same fitting method as Lario et al. (2013), we would have obtained $\sigma = 39.1^\circ$ and $\phi_0 = 11^\circ$. A symmetric Gaussian fit centered on $\phi_0 = 0^\circ$ results in a mean standard deviation

of $\sigma = 35.5^\circ$. The longitudinal distribution of the SEP events, however, is not completely characterized by a standard deviation. Moreover, several factors play an important role, namely the strength of the event and the instrumental background of the detectors. To characterize the actual longitudinal SEP extent at 1 AU, we introduced the longitudinal width of the events, which is described by the range that the fitted curves (Fig. 3) span above a background value (represented by the black horizontal line, which represents a detection limit of 2σ above background). Different from the angular range spanned by the spacecraft that observes the event, the width describes the longitudinal range over which a significant SEP increase was detected during the event. Figure 5 shows the fitted parameters I_0 vs. σ of the wide-spread three-spacecraft events, again excluding fits yielding $|\phi_0| > 90^\circ$. The dashed lines mark longitudinal widths of 180 degrees (black), 300 degrees (red), and 360 degrees (blue). The shaded area cannot be filled by definition of the selection criterion. The widths of our events all lie above 180 degrees, with some of them even exceeding 300 degrees. Figure 6, right, shows the same, but these points are the outcome of Gaussian fits that were forced to be centered on $\phi_0 = 0^\circ$, assuming a symmetric distribution around the best connection angle. The results of the two methods are similar, but the widths of the symmetric Gaussians tend to be larger, even reaching 360° .

4.2. Longitudinal variation of onset delays

Figure 7 displays the SEP onset delay, which is the time between the injection at the Sun (assumed to be the type III burst onset, cf. Fig. 2) and the electron onset at the spacecraft, as a function of the longitudinal separation angle. A correction of ~ 8 min for the light-travel time was applied to the type III burst onset time, so that the onset delay can be seen as the propagation time of the electrons. As in Fig. 3, each color represents an individual event

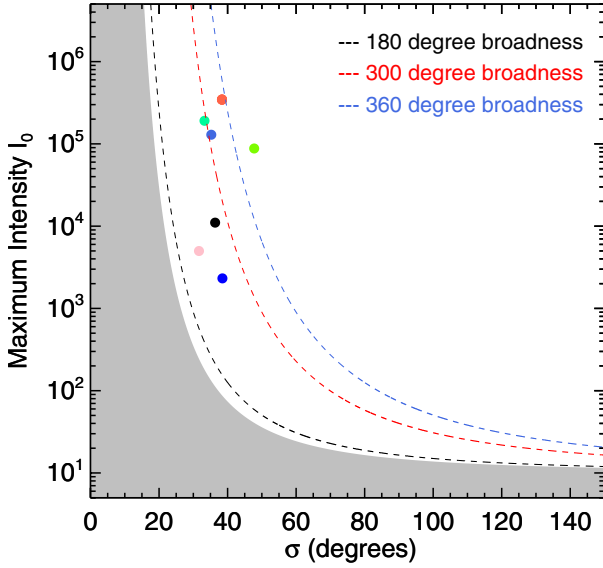


Fig. 5. Parameters I_0 as a function of σ of the fitted curves of Fig. 3 representing the longitudinal widths of the events. Widths of 180 degrees, 300 degrees, and 360 degrees are indicated by dashed lines. The gray shaded area cannot be filled by definition because of the event selection criteria.

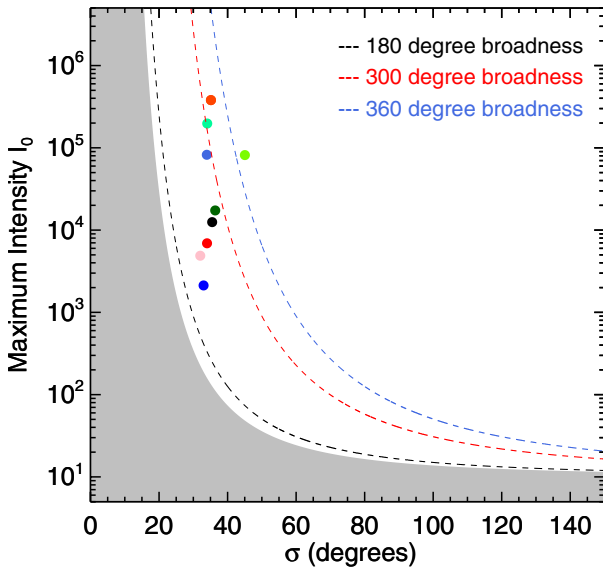


Fig. 6. Same as Fig. 5, but the points were determined using a symmetric Gaussian fit that was forced to be centered on $\phi_0 = 0^\circ$.

and each symbol marks a specific spacecraft. The numbers on the right-hand side vertical axis illustrate the path lengths traveled by 55–105 keV electrons according to the delays shown on the left-hand side vertical axes (assuming these particles were injected at the type III burst onset time). The black horizontal solid line marks the travel time of 55–105 keV electrons along a nominal Parker spiral of 1.18 AU length from the Sun to 1 AU, which is ~ 20 min (using a geometric mean energy of 76 keV and assuming scatter-free propagation). It is evident that most of the points in Fig. 7 lie above that line, meaning that the particles arrive delayed at the spacecraft. While such a delay may be expected for growing longitudinal separations, thinking in terms of perpendicular transport in the IP medium, it is remarkable that several well connected events show delays of up to ~ 30 min, which indicates either a delayed injection or a short mean free

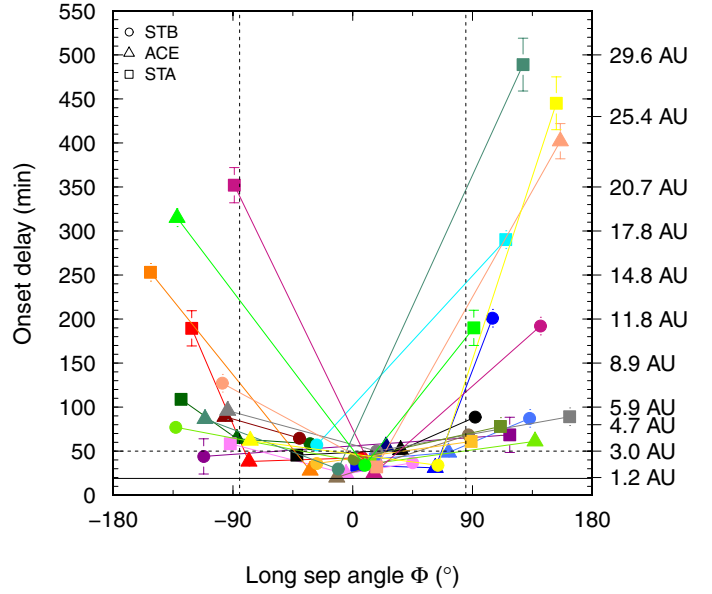


Fig. 7. Onset delay (delay between type III onset and electron onset time at the spacecraft) of the events as function of longitudinal separation angle. A correction of 8.3 min for light-travel time has been applied. The numbers on the right-hand side vertical axis correspond to the distances that the 55–105 keV electrons would travel during the corresponding delay (displayed on the left-hand side vertical axis).

path along the IP magnetic field. Furthermore, strong event-to-event variations can be seen with extreme delays that would give the electrons time to diffusively propagate a distance of up to ~ 30 AU. However, these delays might also be caused by other mechanisms such as a shock, which takes some time to expand and intersect the magnetic field lines connecting to the s/c.

To gain more information on the involved processes, we analyse the anisotropy observed at each of the spacecraft during the same events in Sect. 4.3.

4.3. Longitudinal variation of event anisotropies

The transport of SEPs in the inner heliosphere is determined by a number of physical processes (e.g., Zhang et al. 2009; Dröge et al. 2010). For fast particles such as the electrons considered here, these include advection along the interplanetary magnetic field lines, adiabatic focusing in a diverging magnetic field that tends to drive the particles to the opposite of the parallel gradient in the magnetic field strength, interaction with magnetic field fluctuations that lead to a randomization of the particle pitch angles, diffusion across the average magnetic field, and drift motions due to gradients and curvature in the interplanetary magnetic fields and due to induced electric fields (the latter leading to co-rotation of solar particle events). For slower particles (e.g., ions with energies of a few MeV/n and below) the effects of convection with the solar wind and of adiabatic energy losses are also important, but for the electrons studied here we can safely neglect them. In addition to the processes that govern the injection into the interplanetary medium, the onset of a solar electron event observed on a spacecraft that is magnetically well connected to the acceleration region is then basically determined by the effects of advection, focusing, and pitch-angle diffusion, for events poorly magnetically connected, perpendicular diffusion and co-rotation can be important as well. In large solar particle events, CMEs and interplanetary shock waves frequently lead to distortions in the geometry of the interplanetary magnetic field,

which in some cases can heavily influence the transport of energetic electrons.

The anisotropy of solar particles observed during an event is a crucial parameter for characterizing the properties of their transport. For energetic electrons the anisotropy is mainly determined by the balance between the effect of focusing and the degree of scattering at magnetic fluctuations. If the measurement reveals a strong anisotropy, the particles are assumed to have propagated relatively scatter-free and a good magnetic connection to the source region must have been present. The more scattering the particles experience during their travel, the more isotropic the flux becomes and the directionality is washed out. The anisotropy is typically strongest during the onset of an event while the flux isotropizes during the decay phase. Sometimes a long-lasting injection at the Sun can lead to a persisting anisotropy in the decay phase as well.

To obtain the anisotropy we employed sectorized intensity measurements taken by the STEREO/SEPT and ACE/EPAM instruments, which provide four and eight different viewing sectors. For details see Sect. 2. Anisotropy A is defined as

$$A = \frac{3 \int_{-1}^{+1} I(\mu) \cdot \mu \cdot d\mu}{\int_{-1}^{+1} I(\mu) \cdot d\mu}, \quad (2)$$

where $I(\mu)$ is the pitch-angle-dependent intensity measured in a given viewing direction and μ is the average pitch angle cosine for that direction. Omnidirectional intensities were calculated by integrating second-order polynomial fits to the pitch-angle-dependent intensities $I(\mu)$ using five-minute averages of the data. To stabilize the fit during periods of poor pitch-angle coverage an artificial point was added to the pitch-angle distribution to fill the uncovered range (cf., Dröge et al. 2014). Figure 8 shows STEREO B measurements during the SEP event on 14 August 2010 SEP event, which serves as a good example of an anisotropic event. The upper panel shows the time series of the intensity in color coding as a function of pitch angle. The middle panel shows the 55–105 keV electron intensity measured by the four SEPT telescopes SUN, ANTI-SUN, NORTH, and SOUTH. The third panel shows the anisotropy as deduced from the pitch-angle-dependent intensity measurements. The anisotropy reaches a maximum of 1.93 during the onset of this event. The four panels below show the magnetic field latitudinal and azimuthal angles, the magnetic field magnitude, and the solar wind speed.

The highest anisotropies were now determined for each of the observations of the listed events. To do this, we considered the rising phases of the events alone. If a later contribution by a shock was present, this was not taken into account. Although the anisotropies show an overall dependence on the longitudinal separation angle, the dependence is not as clear as for peak intensities or onset delays. We found different kinds of distributions and therefore separated the events into three classes of comparable observations:

- (1) Significant anisotropy is observed at a well connected spacecraft ($\phi < 50^\circ$), but almost no anisotropy at a far away spacecraft ($A < 0.6$ at $\phi > 60^\circ$, with ϕ being the longitudinal separation angle). The 17 May 2012 event is an example for this class (see Fig. A.1 and discussion below).
- (2) The highest anisotropy is observed by the best-connected spacecraft, but significant anisotropy ($A > 0.6$) is still observed at widely separated positions ($\phi > 60^\circ$). Figure A.2 shows the 11 April 2013 event, serving as an example for class (2).

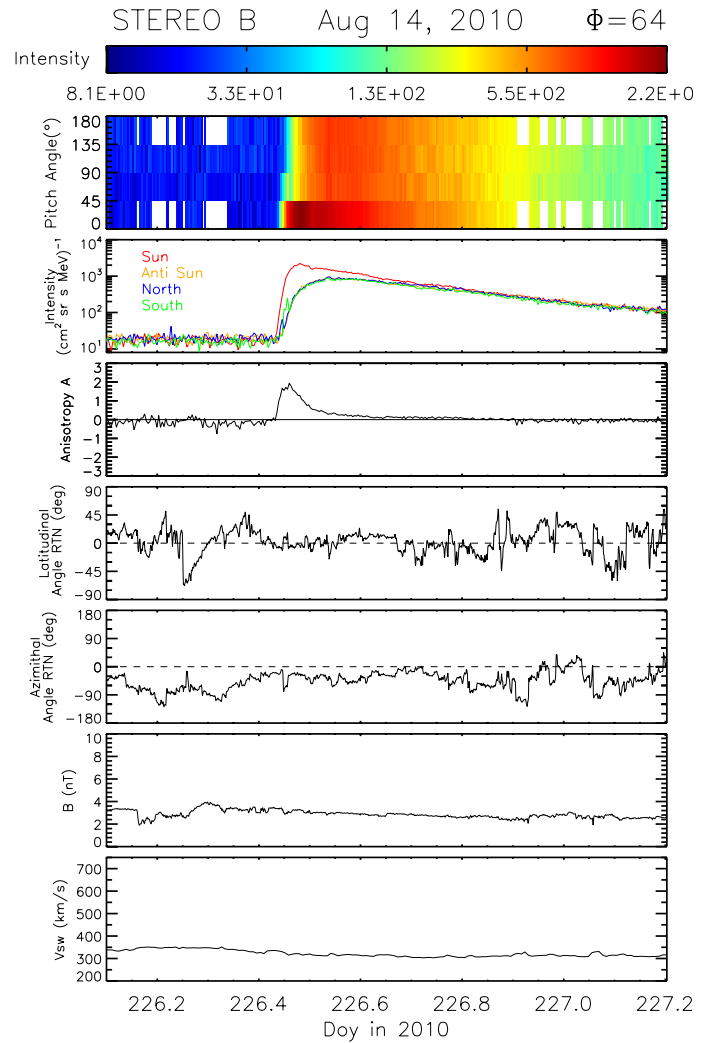


Fig. 8. In-situ observations during the 14 August 2010 SEP event observed by STEREO B. From *top to bottom*: pitch-angle-dependent intensity distribution in color-coding, intensity measured in each of the above telescopes (Sun (red), Anti Sun (orange), North (blue), and South (green)), anisotropy, magnetic field latitudinal and azimuthal angles, magnetic field magnitude, and solar wind speed.

- (3) The highest anisotropy is not observed by the best-connected spacecraft, but by one that is farther away. This is the case of the 14 August 2010 event, presented in Fig. A.3.

For each of these three classes an event serving as an example is shown and discussed in Appendix A. The intensity and anisotropy-time profiles observed at the three spacecraft are shown in Figs. A.1 to A.3.

Figure 9 illustrates the statistics of the absolute anisotropy maxima for the events under study observed by the three spacecraft as a function of longitudinal separation angle. The left panel of Fig. 9 shows the anisotropies of events in class (1), the middle panel the events of class (2), and events of class (3) are shown in the right panel.

Black and red symbol fillings denote good or poor pitch-angle coverage. For poor pitch-angle coverage (< 90 degrees) the anisotropy only serves as lower limit.

Wibberenz & Cane (2006) argued that the onset delays and times to maximum are correlated because of the propagation conditions. Thus Fig. 10 shows the onset delay as a function of the rise time of each event. The events were again separated

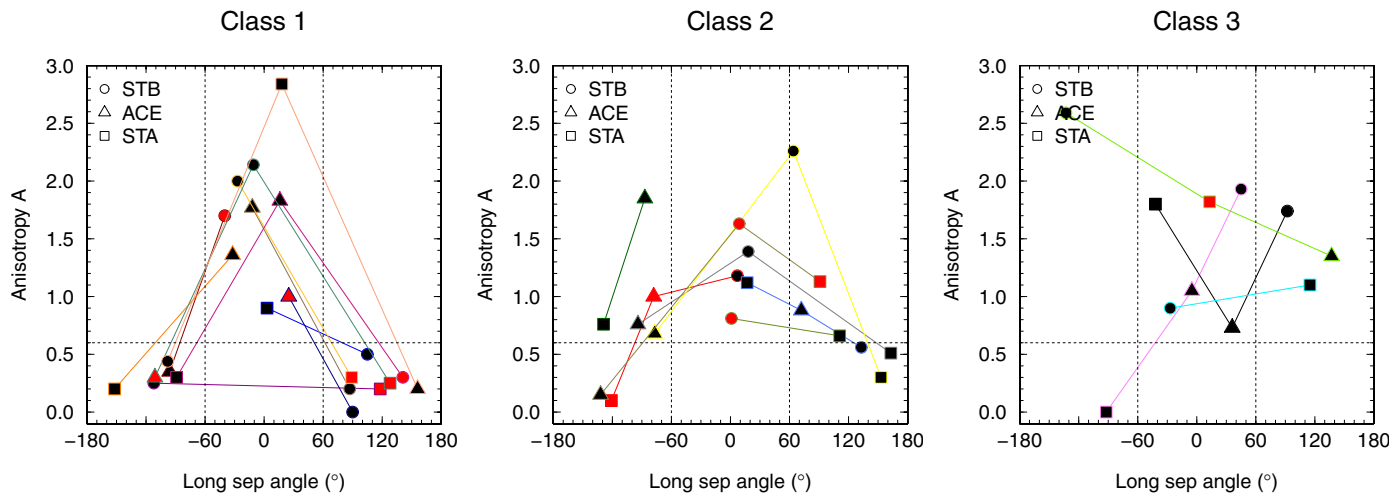


Fig. 9. Maxima of absolute anisotropies observed during the early phases of the events. The observations have been ordered into three different classes (see text) that appear in the *left*, *middle*, and *right* panels. Red symbol fillings denote that the anisotropy may be underestimated because of poor pitch-angle coverage, black fillings mean that the pitch-angle coverage was sufficient. The dashed lines mark the borders that define the different anisotropy classes (see text).

into the three classes as derived from the anisotropy distribution. The Pearson correlation coefficient of each set of points is displayed at the top right of each panel. The points in class (1) show a correlation of $c = 0.76$. Class (2) shows an even stronger correlation of $c = 0.85$. Only the points of class (3) do not correlate ($c = 0.05$). Even if we exclude the point that is far from the rest of the points (onset delay ~ 290 min), the correlation coefficient remains low at $c = 0.34$.

5. Discussion and conclusion

Varying anisotropy distributions can serve as one of the key informations to distinguish source and transport processes. Figure 11 therefore sketches three different source and transport scenarios that agree with the variable anisotropy distributions presented above. While in Fig. 11a just a small source region at the Sun (flare) is present (yellow star), the scenarios in Fig. 11b and c show an extended source region at the Sun (red arc). Such an extended source region may be created by coronal transport (cf. Reinhard & Wibberenz 1974; Newkirk & Wentzel 1978; Klein et al. 2008) and may be supported by a large (coronal) shock (Cliver et al. 1995) and/or an EIT wave (Rouillard et al. 2012; Park et al. 2013). However, none of the suggested lateral transport mechanisms can be favored from our analysis. In all three diagrams red areas mark regions of strong anisotropy, because here the connection to the source is good. This region is very narrow in scenario a). Scenario a) agrees with the observations of anisotropy class (1) (Fig. 9 left). Here, only a well connected observer detects an anisotropic increase, but widely separated spacecraft observe an isotropic event. Thus SEPs reach widely separated positions only through strong perpendicular diffusion, with vanishing anisotropies (represented by the gray areas). The intensity increase at the spacecraft is consequently more gradual here and starts later. The presence of perpendicular transport in the IP medium is represented by the wavy magnetic field lines in the sketches. These stand for wandering magnetic field lines as well as perpendicular diffusion through scattering.

In scenario b) the SEPs are injected over a much wider angular range at the Sun, and under normal conditions particles will arrive at Earth possessing a noticeable anisotropy. The result is therefore a significant anisotropy over a wider longitudinal

extent correlated with the extent of this source region, which agrees with observations in class (2) (Fig. 9 center). Here, the best-connected observer detects the highest anisotropy, but wider separated spacecraft still observe significant anisotropies during the rising phase of the event. The anisotropy is always higher close to the Sun, which is indicated by darker colors in the red and blue areas.

Because the angular distribution of the particles close to the Sun may take some time, we expect a longer onset delay in the outer regions (shaded red and blue in Fig. 9b). If no strong scattering is present, however, a very short rise time is expected. A prolonged injection time can also cause a more gradual increase of the event, however. From field line random walk or an outward weakening source region at the Sun, a region of medium anisotropy is formed (blue areas). Farther out, the situation is the same as in scenario a). In the gray region there is no anisotropy any more because the particles reached these positions by strong scattering.

The anisotropy class (3) comprises all remaining events (Fig. 9 right). These events are more challenging to explain because the best-connected spacecraft does not observe the highest anisotropy, but a wider separated spacecraft does. Scenario c) (Fig. 11c) illustrates one possible situation that might lead to such a situation. Here, an extended source region is also present, but the propagation conditions in the IP medium strongly vary so that a nominally best-connected spacecraft may not observe the highest anisotropy because of a smaller parallel mean free path in this region. A neighboring spacecraft, however, may detect the highest anisotropy because of a rather scatter-free transport to its position. To investigate these varying propagation conditions, detailed modeling is required.

However, pre-event CMEs or large IP flux rope structures might also produce class (3) observations when a better connection to a wider separated spacecraft is provided than to the nominally best-connected one (cf. Richardson et al. 1991; Gómez-Herrero et al. 2006; Leske et al. 2012; Lario et al. 2013). One of our class (3) events is that on 18 August 2010, which has been analysed by Leske et al. (2012), who found that a pre-event CME played a main role for the STEREO A observations. If a specific structure had played a main role, we would expect the peak intensities to follow this changed ordering as well. But just

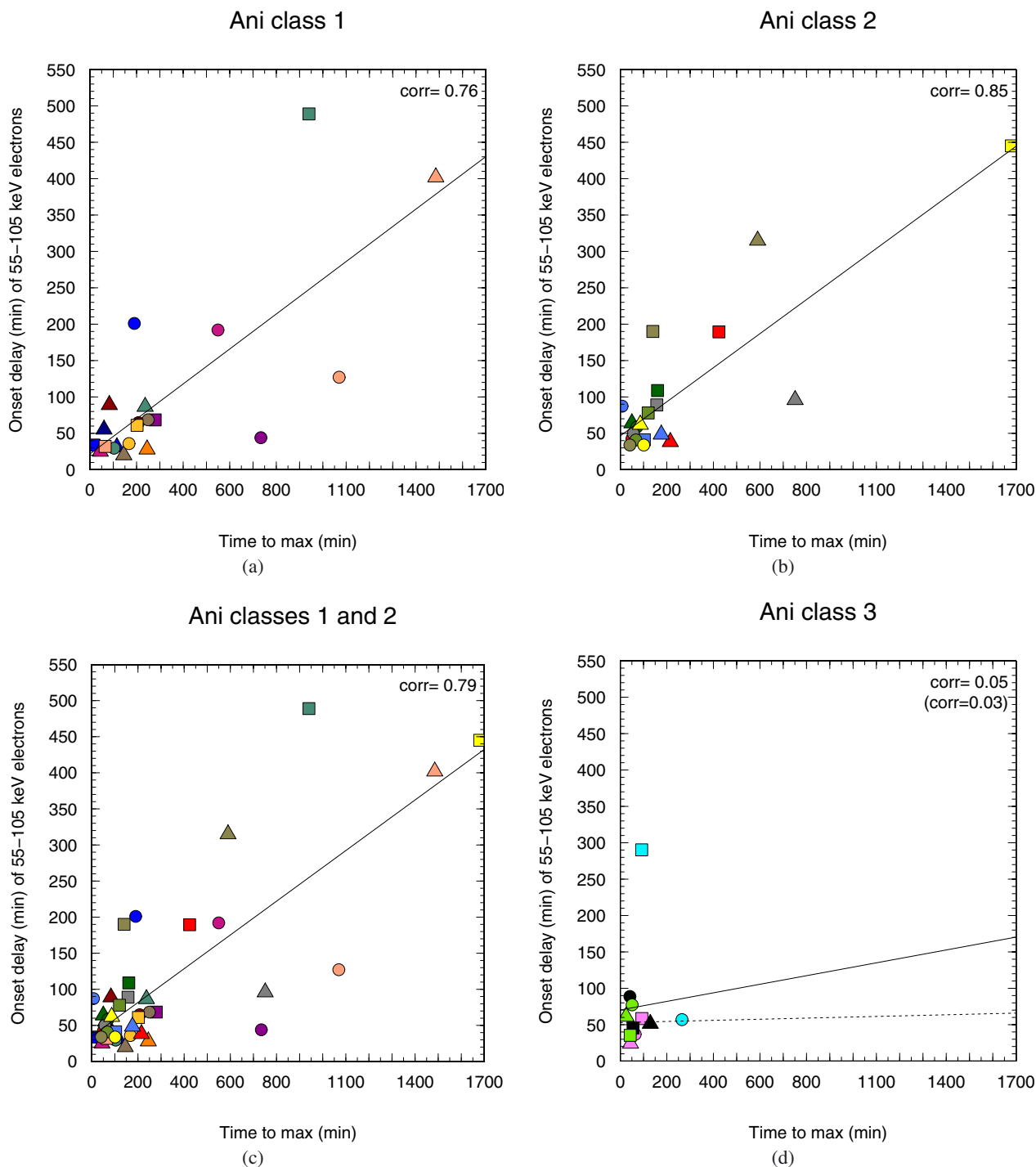


Fig. 10. Onset delay (type III to electron onset) as a function of the rise time of the events. Panel **a**) shows only measurements of class (1), **b**) of class (2), and **d**) of class (3). Panel **c**) combines class (1) and class (2) events. The Pearson correlation coefficient of each group is presented at the top right of each panel, the solid line represents the corresponding fit. The value in brackets of panel **b**) describes the correlation if the yellow point to the right is excluded, the value in brackets in panel **d**) is the correlation when excluding the top cyan point. The dashed line corresponds to these correlations.

one event of the studied sample does not follow the expected ordering in peak intensities, which is the 7 March 2012 event, and it appears in class (1). Another possibility is sympathetic activity, so that the observations at the different spacecraft were not necessarily associated with the same solar event. However, a careful inspection of all available data from optical (EUV) and radio observations suggests that any additional and sympathetic activity can be excluded here. Furthermore, noisy data, local intensity

spikes, and limited pitch-angle coverage can cause varying uncertainties in the anisotropy.

Perpendicular diffusion is known to be a very slow process (Jokipii 1966; Dröge et al. 2010) because of the much smaller perpendicular diffusion coefficient. If strong perpendicular transport is present, the events tend to be more gradual (longer rise times) and start later (longer onset delays). Especially with increasing longitudinal separation angle, these numbers increase

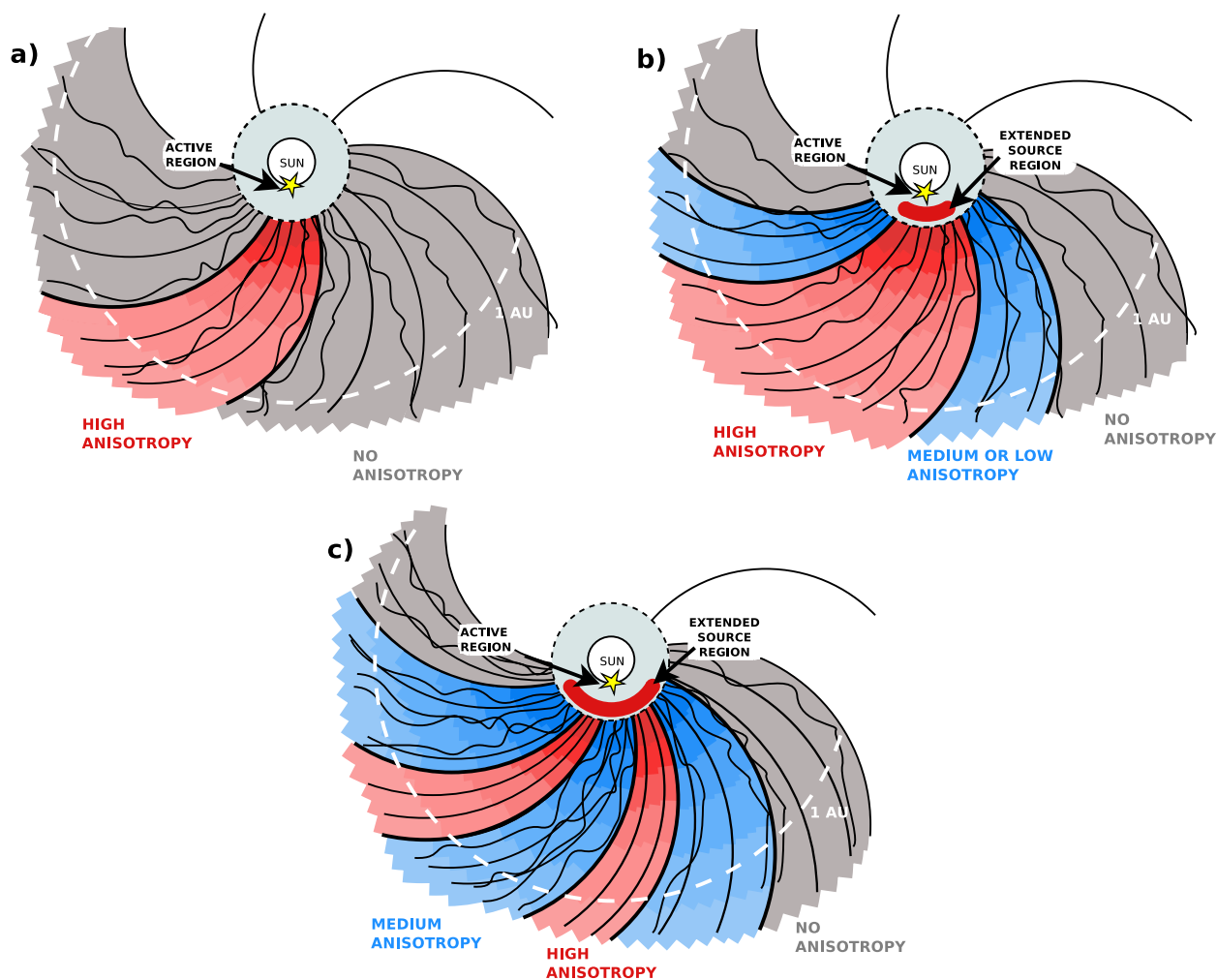


Fig. 11. Regions of varying anisotropy for different source and transport processes. Each diagram describes a wide-spread event extending over all the colored range. While scenario **a)** represents a small source region at the Sun (yellow star), an additional extended source region is present in scenarios **b)** and **c)**, represented by the red arc. Reddish areas mark regions where strong anisotropy is observed, blue regions mark medium anisotropy, and gray areas are regions where no anisotropy can be measured any more. Wavy magnetic field lines represent regions with perpendicular transport in the IP medium.

even more because of the increasing path length of the particles. Thus, we expect the events showing the longest onset delays and rise times to appear in class (1). Furthermore, a correlation between onset times and rise times should be present in class (1). Figure 10 plots these values against each other for the different anisotropy classes. Figure 10a shows only observations of class (1), Fig. 10b of class (2), Fig. 10d of class (3), and Fig. 10c combines class (1) and class (2) events. The longest onset delays and rise times indeed tend to appear in class (1), but class (2) also shows some strongly delayed events. In agreement with our expectations, there is no correlation between onset delays and rise times for class (3) events, probably supporting the idea of large-scale structures in the magnetic field that change the overall geometry. However, although there is some correlation for class (1) events ($c = 0.76$), the same is true for class (2) events, where the correlation coefficient is $c = 0.85$. If a large SEP distribution close to the Sun is the dominant process for the wide spread of class (2) events, we might expect an increasing onset delay with increasing separation angle because the coronal transport to far points may also take some time, but this does not account for an increasing rise time of the events. However, we found no significant difference in the linear fits to class (1) and class (2) events. Nevertheless, the correlations for class (1) and

class (2) as well as any combination of the events in these classes do not change significantly. Therefore, we conclude that both an extended distribution close to the Sun and perpendicular transport in the IP medium exist at the same time (cf. Fig. 11b) for both classes. We therefore expect the limit between class (1) and class (2) to be a smooth one. Whether an event appears in one or the other class only depends upon the individual importance of an extended source vs. perpendicular diffusion, but is also influenced by the specific magnetic connection of the spacecraft and the flaring AR during the event. To investigate the event-to-event variations and the specific dominance of the different mechanisms, detailed modeling of the events is required (e.g. Dröge et al. 2010; Kallenrode et al. 1992; Dröge et al. 2014).

All but one event of our sample are accompanied by a CME. Eighteen out of the 21 events (86%) show an associated type II radio burst that marks the presence of a shock. Interestingly, two of the three events that lack a type II radio burst are class (2) events, suggesting that a shock may not be the key ingredient for the wide SEP distribution close to the Sun. This also was the conclusion by Dröge et al. (2014), who studied one of these events in detail, that of 7 February 2010, and suggested that the lateral transport of the SEPs in this event occurs partially close to the Sun and partially in the IP medium. Furthermore, all of

the events in our sample are accompanied by EIT waves (see Table 1). Recently, Rouillard et al. (2012) and Park et al. (2013) have pointed out that the propagation of an EUV front may be spatially and temporally linked to the SEP release and, therefore, to the observed onset delays. Other authors, however, have questioned this correlation (Miteva et al. 2014) and many EIT waves are observed at well connected positions without any associated SEP increase.

6. Summary

We presented a sample of wide-spread solar (55–105 keV) electron events observed by the two STEREO spacecraft and ACE. We determined a wide-spread event by a longitudinal separation angle of flare to spacecraft magnetic footprint of at least 80 degrees for one spacecraft. The sample contains 21 events from November 2009 to August 2013. The observations were investigated in a statistical manner in terms of peak intensities (Fig. 3), onset delays (Fig. 7), and highest anisotropies (Fig. 9). Assuming a longitudinal SEP distribution of Gaussian shape, we approximated the peak intensities with Gauss functions and found a mean standard deviation of $\sigma = 37.3^\circ$. From the fitted peak intensities and standard deviations we derived the actual longitudinal event widths at 1 AU as the longitudinal ranges spanned by the fitted Gaussians until these reached a characteristic background value. In contrast to the longitudinal range spanned by the spacecraft observing the event, the longitudinal width represents the longitudinal range over which the event is detectable. The widths of the analysed events all lie above 180 degrees, with several events turning out to be ~ 300 degree wide events at 1 AU.

While all events but one showed the expected peak intensity distribution of highest intensity at the best-connected spacecraft and decreasing intensity with increasing separation angle (Fig. 3), the dependence is not as obvious for the onset delays. Although a clear overall dependence on the separation angle is observed in the whole sample, several events show deviations from this, and a strong event-to-event variation is present. Some onsets are even delayed by 300 to 500 min, which corresponds to the time these electrons would need to travel a distance of ~ 20 AU. This corresponds to an effective path length from the Sun to Jupiter.

As a key characteristic we also investigated the longitudinal variation of the highest anisotropies observed at the individual spacecraft during the rise phases of the events. The overall dependence on the longitudinal separation angle is even less clear. To describe the different anisotropy distributions we defined three classes: class (1) comprised events showing high anisotropy at small longitudinal separations ($\phi < 50^\circ$) and no anisotropy at far longitudinal separations ($\phi > 60^\circ$). The observations of this class (Fig. 9 left) agree with what we expect if perpendicular diffusion in the IP medium plays the main role for the particle spread. Events of class (2) also show the highest anisotropy at the best and well connected spacecraft, but significant anisotropy is still observed at a widely separated point ($\phi > 60^\circ$, Fig. 9 center). To obtain such observations a wide SEP distribution close to the Sun is required. Class (3) contains the remaining events, which always show higher anisotropy at a wider separated spacecraft than at the best-connected spacecraft. These events cannot be explained by either only perpendicular diffusion in the IP medium or an extended SEP distribution close to the Sun, but instead are probably produced by specific IP magnetic configurations or by strong spatial variations in the propagation conditions.

For the same classes as defined for the anisotropy distributions we determined the correlation between onset delay and rise time of the events. A correlation of these two parameters is expected if perpendicular diffusion is present. However, although the class (3) events show no correlation, both class (1) and class (2) events show some correlation. This may suggest that even if an extended SEP distribution close to the Sun is needed to explain the observed anisotropies of class (2) events, perpendicular transport is also present. In the same sense it is conceivable that a pre-spreading for the class (1) events occurs already close to the Sun before perpendicular transport in the IP medium sets in. Which mechanisms in detail are responsible for a widening of the SEP distribution close to the Sun is not clear. It may be any coronal transport process, as proposed by Reinhard & Wibberenz (1974); Newkirk & Wentzel (1978); Klein et al. (2008), for example. Recently, EIT waves, which accompany all of our events, have been suggested to be associated with the SEP spread (Rouillard et al. 2012; Park et al. 2013). Furthermore, type II radio bursts as indicators for a shock in 87% of our events, and CMEs, which are almost always present, may be important ingredients.

From our analysis we conclude that wide-spread SEP events are not always produced by the same and only one mechanism, but that different processes are capable of spreading the SEPs over wide longitudinal ranges. We found three different classes of events from considering their anisotropy distributions, which suggest that perpendicular transport in the IP medium on the one hand and a wide particle spread close to the Sun on the other hand play the main roles for most of the events studied here. It is very likely that a combination of these (and probably other) mechanisms influenced the investigated events, but the importance of the different processes may vary from event to event.

Acknowledgements. We acknowledge the STEREO PLASTIC, IMPACT, SECCHI, EIT and Wind teams for providing the data used in this paper. The STEREO/SEPT Chandra/EPHIN and SOHO/EPHIN project is supported under grant 500C1302 by the Federal Ministry of Economics and Technology on the basis of a decision by the German Bundestag. We acknowledge the SEPserver project under grant agreement No. 262773. R. Gómez-Herrero acknowledges financial support from the Spanish Ministerio de Ciencia e Innovación under project AYA2011-29727-C02-01. Y.K. was also partially supported by program No. 22 of the Russian Academy of Sciences.

References

- Acuña, M. H., Curtis, D., Scheifele, J. L., et al. 2007, *Space Sci. Rev.*, 136, 203
- Bougeret, J. L., Kaiser, M. L., Kellogg, P. J., et al. 1995, *Space Sci. Rev.*, 71, 231
- Bougeret, J. L., Goetz, K., Kaiser, M. L., et al. 2008, *Space Sci. Rev.*, 136, 487
- Brueckner, G. E., Howard, R. A., Koomen, M. J., et al. 1995, *Sol. Phys.*, 162, 357
- Cane, H. V., McGuire, R. E., & von Roseninge, T. T. 1986, *ApJ*, 301, 448
- Cliver, E. W., Kahler, S. W., Neidig, D. F., et al. 1995, in *Proc. 24th International Cosmic Ray Conference (Rome)*, 4, 257
- Cliver, E. W., Thompson, B. J., Lawrence, G. R., et al. 2005, in *Proc. 29th International Cosmic Ray Conference (Pune)*, 1, 121
- Dalla, S., Balogh, A., Krucker, S., et al. 2003, *Geophys. Res. Lett.*, 30, 8035
- Dresing, N., Gómez-Herrero, R., Klassen, A., et al. 2012, *Sol. Phys.*, 281, 281
- Dresing, N., Gómez-Herrero, R., Klassen, A., et al. 2013, in *Proc. 33rd Internat. Cosmic Ray Conf. (Rio de Janeiro)*, paper 0611
- Dröge, W., Kartavykh, Y. Y., Klecker, B., & Kovaltsov, G. A. 2010, *ApJ*, 709, 912
- Dröge, W., Kartavykh, Y. Y., Dresing, N., Heber, B., & Klassen, A. 2014, *J. Geophys. Res.*, submitted
- Galvin, A. B., Kistler, L. M., Popecki, M. A., et al. 2008, *Space Sci. Rev.*, 136, 437
- Gold, R. E., Krimigis, S. M., Hawkins, I. I. I., S. E., et al. 1998, *Space Sci. Rev.*, 86, 541
- Gómez-Herrero, R., Klassen, A., Müller-Mellin, R., Heber, B., & Wimmer-Schweingruber, R. F. 2006, in *SOHO-17, 10 Years of SOHO and Beyond*, ESA SP, 617, CD-ROM id. 128.1

- Gopalswamy, N., Xie, H., Akiyama, S., et al. 2013, *ApJ*, 765, L30
- Heber, B., Dresing, N., Dröge, W., et al. 2013, in *Proc. 33rd Internat. Cosmic Ray Conf. (Rio de Janeiro)*, paper 0746
- Howard, R. A., Moses, J. D., Vourlidas, A., et al. 2008, *Space Sci. Rev.*, 136, 67
- Hsieh, K. C., & Simpson, J. A. 1970, *ApJ*, 162, L191
- Jokipii, J. R. 1966, *ApJ*, 146, 480
- Kallenrode, M.-B. 1993, *J. Geophys. Res.*, 98, 5573
- Kallenrode, M.-B., Wibberenz, G., & Hucke, S. 1992, *ApJ*, 394, 351
- Klassen, A., Gómez-Herrero, R., Heber, B., et al. 2012, *A&A*, 542, A28
- Klein, K.-L., Krucker, S., Lointier, G., & Kerdraon, A. 2008, *A&A*, 486, 589
- Krucker, S., Larson, D. E., Lin, R. P., & Thompson, B. J. 1999, *ApJ*, 519, 864
- Laitinen, T., Dalla, S., & Marsh, M. S. 2013, *ApJ*, 773, L29
- Lario, D., Aran, A., Gómez-Herrero, R., et al. 2013, *ApJ*, 767, 41
- Lemen, J. R., Title, A. M., Akin, D. J., et al. 2012, *Sol. Phys.*, 275, 17
- Leske, R. A., Cohen, C. M. S., Mewaldt, R. A., et al. 2012, *Sol. Phys.*, 281, 301
- Lin, R. P., & Hudson, H. S. 1976, *Sol. Phys.*, 50, 153
- Marsh, M. S., Dalla, S., Kelly, J., & Laitinen, T. 2013, *ApJ*, 774, 4
- Mason, G. M., Gloeckler, G., & Hovestadt, D. 1984, *ApJ*, 280, 902
- McComas, D. J., Bame, S. J., Barker, P., et al. 1998, *Space Sci. Rev.*, 86, 563
- Miteva, R., Klein, K.-L., Kienreich, I., et al. 2014, *Sol. Phys.*, 289, 2601
- Moses, D., Clette, F., Delaboudinière, J.-P., et al. 1997, *Sol. Phys.*, 175, 571
- Müller-Mellin, R., Böttcher, S., Falenski, J., et al. 2008, *Space Sci. Rev.*, 136, 363
- Newkirk, Jr., G., & Wentzel, D. G. 1978, *J. Geophys. Res.*, 83, 2009
- Papaioannou, A., Souvatzoglou, G., Paschalis, P., Gerontidou, M., & Mavromichalaki, H. 2014, *Sol. Phys.*, 289, 423
- Park, J., Innes, D. E., Bucik, R., & Moon, Y.-J. 2013, *ApJ*, 779, 184
- Reames, D. V. 1999, *Space Sci. Rev.*, 90, 413
- Reinhard, R., & Wibberenz, G. 1974, *Sol. Phys.*, 36, 473
- Richardson, I. G., Cane, H. V., & von Rosenvinge, T. T. 1991, *J. Geophys. Res.*, 96, 7853
- Rouillard, A. P., Sheeley, N. R., Tylka, A., et al. 2012, *ApJ*, 752, 44
- Smith, C. W., L'Heureux, J., Ness, N. F., et al. 1998, *Space Sci. Rev.*, 86, 613
- Thompson, B. J., Plunkett, S. P., Gurman, J. B., et al. 1998, *Geophys. Res. Lett.*, 25, 2465
- Torsti, J., Kocharov, L., Teittinen, M., et al. 1999, *J. Geophys. Res.*, 104, 9903
- Wibberenz, G., & Cane, H. V. 2006, *ApJ*, 650, 1199
- Wiedenbeck, M. E., Mason, G. M., Cohen, C. M. S., et al. 2013, *ApJ*, 762, 54
- Zhang, M., Qin, G., & Rassoul, H. 2009, *ApJ*, 692, 109

Appendix A: Anisotropy– and intensity–time profiles during three example events

In the following, we show three example events for the three anisotropy classes defined in Sect. 4.3. Multipoint observations of both STEREO spacecraft and ACE are shown for each of the three events in Figs. A.1 to A.3. The figures always present from top to bottom the time series of the intensity in color coding as a function of pitch angle, the pitch angle of each of the four SEPT telescopes, the 55–105 keV electron intensity as measured in the four telescopes, and the anisotropy.

A.1. Class-1 example: the SEP event on 17 May 2012

Figure A.1 presents observations of the event on 17 May 2012, which was the first ground-level enhancement (GLE) of solar cycle 24 (Heber et al. 2013; Gopalswamy et al. 2013; Papaioannou et al. 2014). While ACE (shown in the middle figure) was well connected to the source flaring AR ($\Phi = 16$) and observed a clear anisotropic event, STEREO A and B were separated by 89 and 141 degrees. Although both STEREO spacecraft detected a significant intensity increase, both increases are rather isotropic.

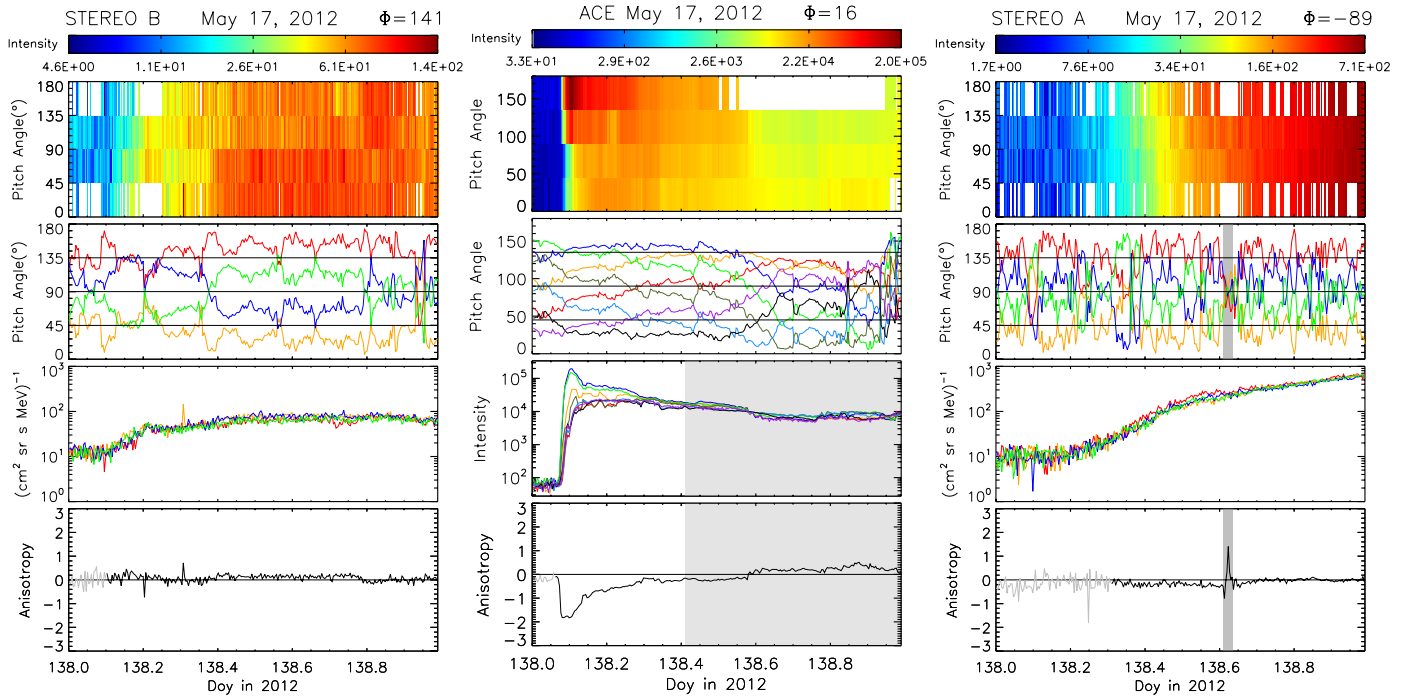


Fig. A.1. Anisotropy and intensity time profiles of the SEP event on 17 May 2012 observed by STEREO B (*left*), ACE (*middle*), and STEREO A (*right*). Anisotropy plotted in lighter color denotes periods of background intensity for which the anisotropy calculation is very uncertain. Gray shading in ACE observations marks a period where the electron measurements (and following the anisotropy) are contaminated by ions. The small shaded area in STEREO A measurements denotes a period of very poor pitch-angle coverage, which led to an incorrect anisotropy determination.

A.2. Class-2 example: the SEP event on 11 April 2013

Figure A.2 shows the event on 11 April 2013 where an angular widely separated spacecraft (ACE) still observed significant anisotropy. Here, STEREO B (middle figure) is the best-connected spacecraft ($\Phi = 64$), and ACE and STEREO A are separated by 77 and 153 degrees.

A.3. Class-3 example: the SEP event on 14 August 2010

The event shown in Fig. A.3 occurred on 14 August 2010. Although ACE (middle figure) was the best-connected spacecraft ($\Phi = -5^\circ$) and observed the highest intensity, and although the footpoint of STEREO B was 15° away from the flare longitude, STEREO B observed stronger anisotropy. The absolute highest anisotropy is 1.93, which is twice the value observed by ACE (1.05). Interestingly enough, STEREO A, separated by 92 degrees, observed no significant anisotropy during this event.

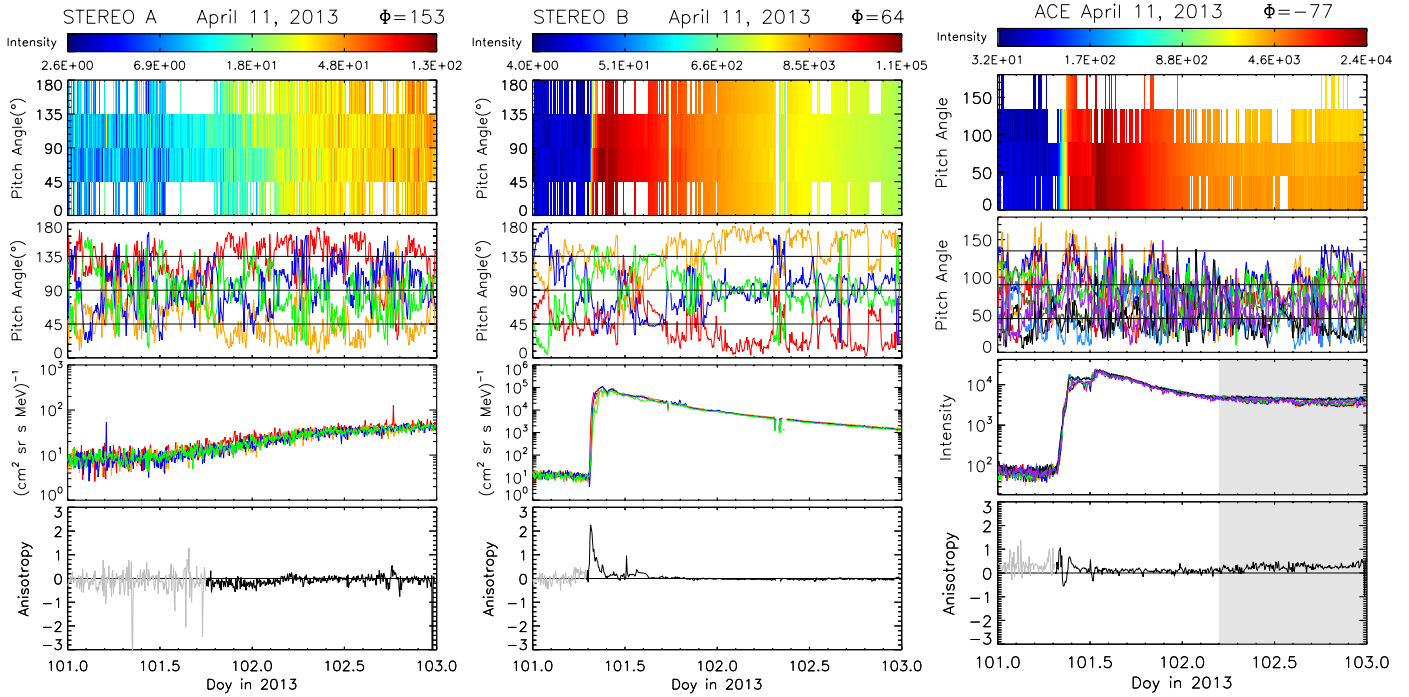


Fig. A.2. Anisotropy and intensity time profiles of the SEP event on 11 April 2013 observed by STEREO A (*left*), STEREO B (*middle*), and ACE (*right*). Anisotropy plotted in lighter color denotes periods of background intensity for which the anisotropy calculation is very uncertain. The gray-shaded area in the ACE plot marks a period of ion contamination.

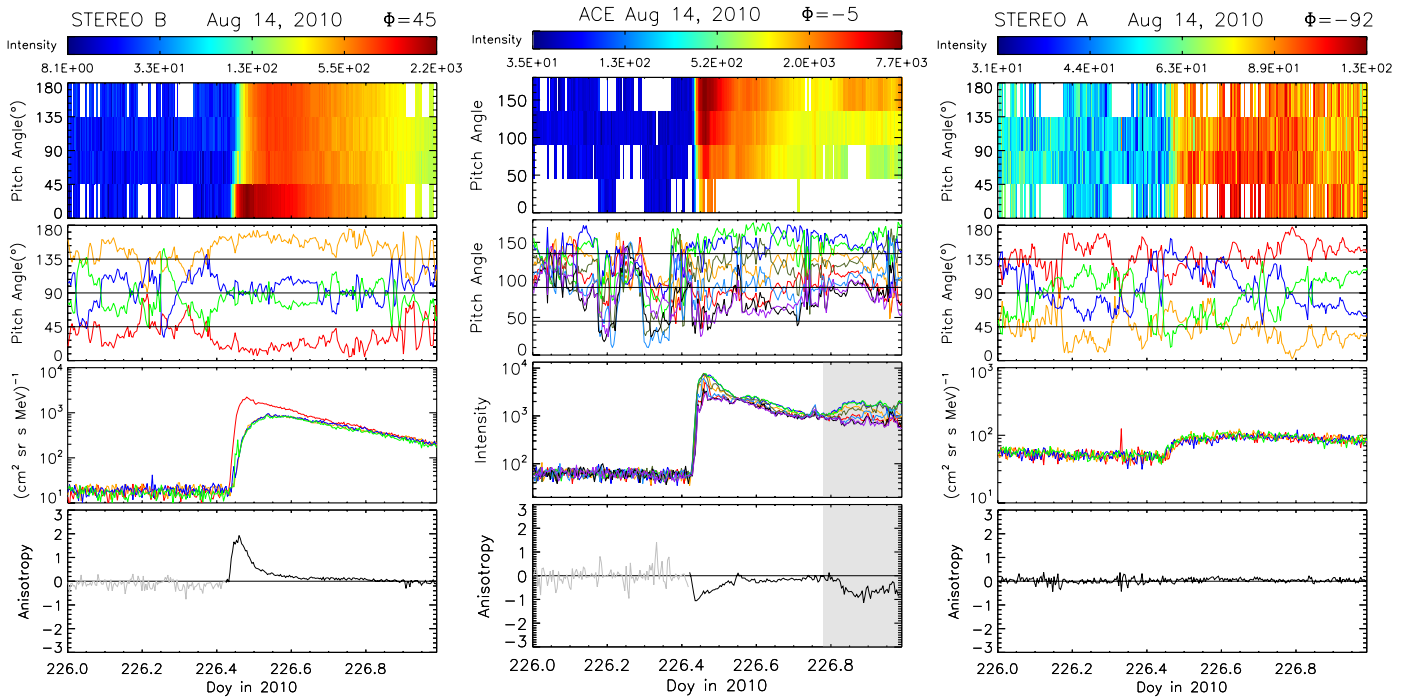


Fig. A.3. Anisotropy and intensity time profiles of the SEP event on 14 August 2010 observed by STEREO B (*left*), ACE (*middle*), and STEREO A (*right*). Anisotropy plotted in lighter color denotes periods of background intensity for which the anisotropy calculation is very uncertain. The gray-shaded area in ACE anisotropy and intensity marks a period of ion contamination that saturated the electron measurements and led to an incorrect anisotropy determination.